Progress on laser ignition simulations of a CH_4/O_2 subscale rocket combustor using a multi-GPU task-based solver

By J. M. Wang, M. Di Renzo†, C. Williams, J. Urzay AND G. Iaccarino

1. Motivation and objectives

The prediction of reliability of laser ignition in a gaseous methane (CH_4)/molecular-oxygen (O_2) subscale rocket combustor, using multifidelity ensembles of numerical simulations running on exascale-class supercomputers, is the overarching goal of the Stanford PSAAP-III Center (2020–2025). This report describes progress made on numerical simulations using a multi-node task-based solver built on the Legion/Regent software stack during the first year of operation of the Stanford PSAAP-III Center. Instead of deploying high-fidelity models from start, particular emphasis was placed in the first year on developing a minimally viable, continuously integrated software framework from the cradle, which could perform simulations of laser ignition with simple models at scale on heterogeneous supercomputers (CPUs+GPUs) and could be portable across multiple platforms. Subsequent years will focus on refinements of this computational tool along with augmentation of the numerics and the elementary models employed in this report.

Laser ignition systems are experimental technologies under active research in space industry for re-startable rocket engines and reaction control thrusters in upper stages, spacecrafts, and satellites (Kroupa & Börner 2018). A laser pulse of approximately 10 ns duration, with a wavelength of about 1 μm, is focused into a small spot of 10–100 μm of diameter in the rocket combustor, delivering a power density of 10–100 GW/cm^2 and producing a kernel of hot gas of approximately 1 mm in diameter.

Lasers have advantages over traditional ignition technologies like pyrophoric, pyrotechnic, or augmented-torch igniter systems. Pyrophoric ignition consists of mixing hypergolic fluids to produce ignition and has been used widely because of its simplicity and reliability (e.g., in Falcon-9, Soyuz, and Apollo Lunar Excursion Module). However, propellants like triethyl-aluminum/triethyl-borane, unsymmetrical dimethyl-hydrazine, and nitrogen tetroxide are highly toxic and expensive. Pyrotechnic ignition is limited to rocket motors (e.g., the Space Shuttle's solid rocket boosters). Neither pyrophoric nor pyrotechnic ignition methods are capable of many ignition cycles. Augmented-torch ignition systems allow for multiple burns (e.g., Saturn V's J-2 engines and Starship's Raptor engines), but they require a pre-chamber with a bulky spark igniter that is mounted fixed in space and inefficiently releases a large amount of energy over a large gas volume.

In contrast, laser ignition systems provide re-startability, non-intrusiveness, localization of energy deposition, mechanical simplicity, and decoupling from engine transients. Specifically, a large number of re-starts can be achieved with laser ignition systems in space missions requiring multiple burns for insertion of spacecrafts into orbit or for modification of attitude of satellites in orbit. Similarly, laser ignition systems do not require

† CERFACS, France

torches, pre-chambers, toxic hypergolic propellants, or massive electrode components from spark plugs that can act as heat sinks and quench the flame. The energy deposited by the laser can be localized both spatially and temporally in the combustor, thereby providing the capability of initiating the ignition kernel in regions of the flow where the fuel/oxidizer mixture flammability characteristics are favorable for combustion. Additionally, laser ignition systems operate during engine starts independently of propellant flow transients and resonant instabilities caused by pressure coupling with feed lines.

From a fundamental standpoint, flame ignition induced by lasers or similar concentrated sources has been studied theoretically, computationally, and experimentally in stagnant mixtures (Morsy & Chung 2002; Phuoc 2006; Kurdyumov *et al.* 2004; Munafò *et al.* 2019; Wang *et al.* 2021), turbulent jet flames (Wermer *et al.* 2017; De Oliveira 2019; Jo & Gore 2022), gas-turbine engines (Eyssartier *et al.* 2013; Marrero-Santiago *et al.* 2020), supersonic combustors (Brieschenk *et al.* 2014), and rocket combustors (Lacaze *et al.* 2009; Manfletti 2014). Still, understanding of the effects of local flow conditions, including turbulence, shock waves, and sprays, on the success or failure of the ignition sequence remains an open challenge. As a first step toward a LOX-based system typical of liquid rockets, which requires significantly more complex physics models, the present investigation examines forced ignition of a gaseous CH_4/O_2 model rocket combustor. Rather than detail the early flame-growth dynamics, focus will be on combustor-scale dynamics. Due to computational expense, simplified models for the chemistry and laser-energy deposition are used and will be refined in upcoming efforts. A parallel experimental validation effort in this configuration, deferred to future reports, is currently underway at the Zucrow Propulsion Laboratory at Purdue University.

The remainder of this report is structured as follows. Section 2 focuses on the computational set-up. Main simulation results and code performance are discussed in Section 3. Lastly, conclusions are given in Section 4.

2. Formulation and computational set-up

2.1. *Solver*

The simulations highlighted below are conducted using the Hypersonics Task-based Research (HTR) solver described in Di Renzo *et al.* (2020) and developed as part of the Stanford PSAAP-II Center (2014–2020) for compressible chemically reacting flows in simple geometries. The HTR solver is based on the task-based environment Legion, which enables efficient memory management along with an improved mapping of the workload on computer nodes at runtime (Bauer *et al.* 2012). This leads to high scalability in GPU-based supercomputers and allows for the exploitation of heterogeneous architectures (CPU+GPU) without making machine-tailored modifications of the solver. The HTR solver is written in a combination of C++ and the programming language Regent, which is specifically designed to interact with Legion (Slaughter *et al.* 2015). The HTR solver has been verified and validated with a number of canonical shock-tube, boundary-layer, and laminar premixed flame cases, and has been employed in direct numerical simulations of hypersonic boundary layers with thermochemistry (Di Renzo *et al.* 2020; Di Renzo & Urzay 2021).

2.2. *Physical models*

In these simulations, the compressible chemically reacting Navier–Stokes equations are integrated along with mixture-averaged, temperature-dependent thermophysical and trans-

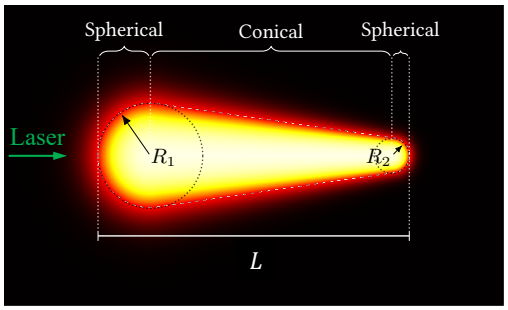

FIGURE 1. Laser-energy kernel geometry with two hemispherical lobes. Brighter color indicates higher temperatures. The laser beam originates from the left.

port properties. Specifically, the thermophysical properties are modeled with the 9-coefficient NASA parameterization of McBride *et al.* (2002) extended to higher post-deposition temperatures using the rigid-rotor harmonic-oscillator approximation (Mayer & Mayer 1959). The transport properties are computed from kinetic theory, as explained by Di Renzo *et al.* (2020) and other standard references in the literature of multicomponent systems. The combustion kinetics are modeled with a single irreversible reaction $CH_4 + 2\,O_2 \longrightarrow 2\,H_2O + CO_2$ with an Arrhenius rate constant whose exponential pre-factor and activation energy are fixed at $1.1 \cdot 10^{10}$ cm^6/mol^2/s and 20 kcal/mol, respectively, as proposed by CERFACS†. More sophisticated kinetic descriptions, ranging from detailed mechanisms to a single step with variable activation energy by Fernández-Tarrazo *et al.* (2006), would provide increasingly relevant results but are deferred to future studies where comparisons with experimental data will be reported.

The energy deposition is modeled as a source term $\dot{Q}_L = \rho \dot{e}_L f(\boldsymbol{x};\, L, R_1, R_2)\, g(t;\, t_L, \tau_L)$ on the right hand side of the total energy equation, where ρ is the fluid density. In this formulation, $0 \leq f(\boldsymbol{x};\, L, R_1, R_2) \leq 1$ is a function that spatially delimits the kernel shown in Figure 1; R_1, R_2, and L are based on CH_4-ignition experiments by Phuoc & White (2002). Additionally, $g(t; t_L, \Delta t_L) = \exp\left\{-(t - t_L)^2/[2(\Delta t_L)^2]\right\}$ is a Gaussian time window, where t_L is the time of laser deployment and Δt_L is a characteristic duration of the pulse that is much smaller than the characteristic sound-crossing time across the kernel. Lastly, the parameter $\dot{e}_L$ corresponds to the peak thermal power deposited per unit mass and is used to control the total energy deposited in the kernel volume $E_L = \int\int \dot{Q}_L dV dt$, which is of the order of millijoules in the simulations highlighted in Section 3.

While this model simplifies the complex laser-plasma interaction described by Munafò *et al.* (2019) and Alberti *et al.* (2020), it captures the non-spherical geometry of the resulting energy kernel, which has a significant impact on the distribution of hot gas during the subsequent flame-kernel growth. In particular, asymmetry of the kernel in the direction of the laser beam (Glumac *et al.* 2005; Zeldovich & Raizer 1966) leads to generation of vorticity, which can transport heated gas to distances several times the initial kernel size (Harilal *et al.* 2015; Wang *et al.* 2020, 2021). It is also anticipated that this laser-generated flow may compete with the background flow in the combustor. Ionized species are excluded in the present study, as they are anticipated to be short-lived ($t \lesssim 10\,\mu$s) (MacArt *et al.* 2021) compared to the combustor-scale ignition dynamics.

† Accessed on 10/27/2021: `http://www.cerfacs.fr/cantera/mechanisms/meth.php#1S`

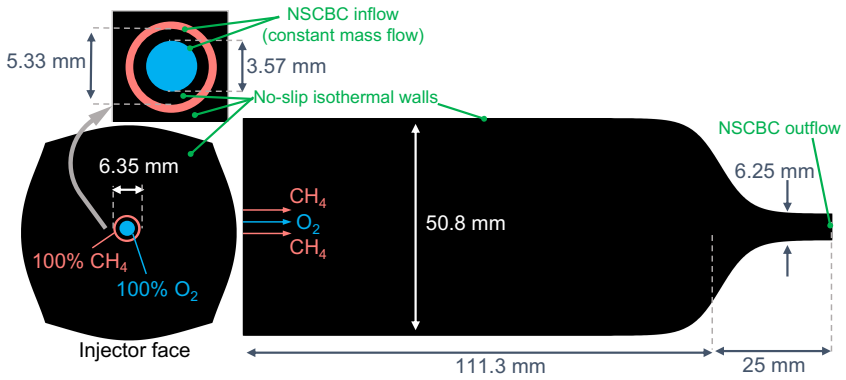

FIGURE 2. Cross-flow and streamwise cross sections of the computational domain showing the injector face, combustion chamber, and nozzle, along with corresponding dimensions.

2.3. *Computational domain, boundary conditions, and numerics*

The computational domain consists of a 111.3 mm × 50.8 mm × 50.8 mm combustion chamber and a converging nozzle with length 25 mm and area ratio 64 to 1, as depicted in Figure 2. Gaseous, pure CH_4 (coflow) and O_2 (center core) are injected through a shear coaxial injector into an initially stagnant, O_2-filled combustor at uniform pressure 137.5 kPa and temperature 300 K. The two streams are separated by an annular wall. The inlet velocity profile is prescribed as

$$U(r) = \begin{cases} U_{O_2} \tanh\left[(R_j - r)/w\right]; & r < R_j \quad \text{(center core)} \\ 0; & R_j \le r \le R_i \quad \text{(injector post)} \\ U_{CH_4} \tanh\left[(R_i - r)/w\right] \tanh\left[(r - R_o)/w\right]; & R_i < r \le D/2 \quad \text{(coflow)} \\ 0; & r > R_o \quad \text{(backplate)} \end{cases}$$

where $r^2 = y^2 + z^2$ is the radial distance from the centerline, $w = 0.03R_o$ is a prescribed parameter, $R_j = 1.78$ mm is the O_2 jet radius, and $R_i = 2.66$ mm and $R_o = 3.17$ mm are, respectively, the inner and outer radii of the CH_4 coflow. The mass flow rate of both CH_4 and O_2 streams is held constant throughout the simulation. Initially, the Mach numbers of CH_4 and O_2 at injection are 0.4 and 1.0, respectively. However, as the chamber pressure increases due to priming and the subsequent ignition, the gas density at the injector orifice also increases, and the velocity of the two streams is decreased such that constant mass flow rates are maintained. In these conditions, the jet Reynolds number based on the O_2-jet velocity and diameter is approximately 66,000. Table 1 summarizes the operating parameters, whose values are set by a parallel experimental validation effort.

The boundary conditions used in the simulations are also indicated in Figure 2. In particular, Navier–Stokes characteristic boundary conditions (NSCBC) described by Poinsot & Lele (1992) and Okong'o & Bellan (2002) are used at the injector inlet and nozzle outflow. The time-varying inflow condition has a velocity profile that is scaled at each time step such that the total mass flow rates of CH_4 and O_2 are constant in time. All walls of the combustor are modeled as no-slip isothermal walls at 300 K. The wall probe locations indicated in Figure 3(b) are used to record local pressure time traces.

The conservation equations are time-integrated using a third-order strong-stability-preserving explicit Runge–Kutta scheme (Gottlieb *et al.* 2001) and discretized in conservative form on a curvilinear mesh using a sixth-order targeted essentially non-oscillatory (TENO) scheme (Fu *et al.* 2016). While initial laser-energy deposition requires a small

Initial chamber pressure	137.5 kPa
Initial chamber temperature	300 K
Initial O_2 Mach number	1.0
Initial CH_4 Mach number	0.44
Initial O_2 injection velocity	295 m/s
Initial CH_4 injection velocity	191 m/s
Constant O_2 injection temperature	242 K
Constant CH_4 injection temperature	282 K
Constant O_2 mass flow rate	6.44 g/s
Constant CH_4 mass flow rate	1.66 g/s
Time of laser deployment, t_L	2.9 ms
Laser pulse duration, Δt_L	4.2 ns
Laser kernel length, L	1.6 mm
Laser kernel small lobe radius, R_1	0.25 mm
Laser kernel large lobe radius, R_2	0.17 mm
Axial location of laser deployment, x_L	12.7 mm

TABLE 1. Main operating parameters.

time step ($\Delta t = 0.2$ ns) to resolve, this stage is very short (10 ns) and does not incur significant computational expense.

The curvilinear grid topology employed in the simulations is shown in Figure 3. Specifically, the grid is constructed using the coordinate transformation

$$x = L_x\hat{\xi} + Af(\hat{\xi})\left(\hat{\eta}^2 + \hat{\zeta}^2\right),$$

$$y = \Big\{R_n\sigma(x/L_x) + R_c\left[1-\sigma(x/L_x)\right]\Big\}\Big\{\mathcal{S}(\eta,\zeta)\sigma(x/L_x) + \mathcal{S}(\hat{\eta},\hat{\zeta})\left[1-\sigma(x/L_x)\right]\Big\},$$

$$z = \Big\{R_n\sigma(x/L_x) + R_c\left[1-\sigma(x/L_x)\right]\Big\}\Big\{\mathcal{S}(\zeta,\eta)\sigma(x/L_x) + \mathcal{S}(\hat{\zeta},\hat{\eta})\left[1-\sigma(x/L_x)\right]\Big\},$$

where $\mathcal{S}(\eta,\zeta) = \zeta\sqrt{(\eta^2+\zeta^2-0.8\eta^2\zeta^2)/(\eta^2+\zeta^2)}$ is a function that partially circularizes the combustor contour (Fong 2018). In addition, the parameters $A = 0.5R_n$, $R_n = 3.12$ mm, and $R_c = 25.4$ mm are used; R_n and R_c correspond to the radius of the nozzle and combustion chamber, respectively. The sigmoid function $\sigma(s)$ is defined as $\sigma(s) = (1/2)\{1+\tanh[20(s-L_c/L_x)]\}$, where $L_x = 136.3$ mm and $L_c = 111.3$ mm are the lengths of the combustor with and without the nozzle, respectively. The curvilinear coordinates $0 \le \xi \le 1$, $-1 \le \eta \le 1$, and $-1 \le \zeta \le 1$ are uniformly spaced. The symbols $\hat{\xi}$, $\hat{\eta}$, and $\hat{\zeta}$ denote stretched coordinates defined as

$$\hat{\xi} = 1 - \frac{\tanh\left[a(1-\xi)\right]}{\tanh(a)}, \qquad \hat{\eta} = 1 - \frac{\sinh\left[b(1-\eta)\right]}{\sinh(b)}, \qquad \hat{\zeta} = 1 - \frac{\sinh\left[b(1-\zeta)\right]}{\sinh(b)},$$

where $a = 0.89$ and $b = 2$ are stretching parameters in the streamwise and transverse directions, respectively.

The mesh has 98 million points ($960 \times 320 \times 320$) and a minimum grid spacing $\Delta x = \Delta y = \Delta z = 88$ μm at the injector orifice, which corresponds to 40 points across the O_2 jet, 10 points across the annular wall, 6 points across the CH_4 coflow. The grid is under-resolved with respect to the premixed laminar flame thickness, which is 91 μm for a stoichiometric CH_4/O_2 mixture at atmospheric pressure, and also with respect to the

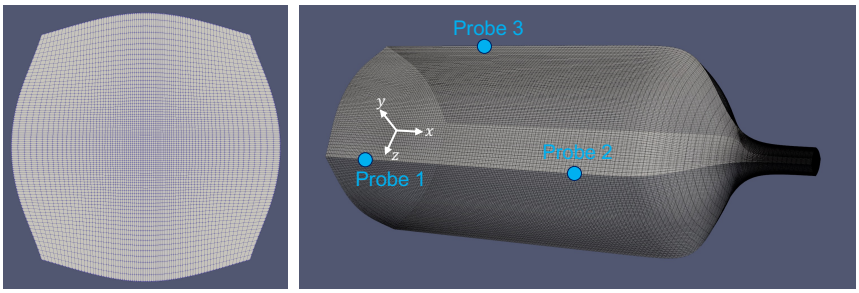

FIGURE 3. Grid topology for (a) the injector face and (b) the full combustor. Every sixth grid point in each direction is shown in this figure. Wall probe locations are shown in (b); probes 1, 2, and 3 are located on the wall at $x = 12.9\,\text{mm}$, $x = 76.4\,\text{mm}$, and $x = 39.9\,\text{mm}$, respectively.

Kolmogorov length scale, which is estimated to be 2 μm using the methods described by Pope (2000) and Panchapakesan & Lumley (1993) for turbulent jets. Due to the large dimensions of the combustor relative to these small scales, a fully resolved simulation would require approximately 100 billion grid points even with stretching, which represents a significant computational endeavor for the long time horizons necessary to obtain a stable flame. As a preliminary measure to maintain positivity of partial species densities at this coarse grid resolution, a flux limiter similar to that of Hu *et al.* (2013) was used during the cold-flow injection stage, while for the ignition stage partial blending of first-order upwinding with the baseline sixth-order TENO scheme was employed. The incorporation of subgrid-scale and turbulent combustion models in these simulations, coupled with appropriate numerical schemes and Legion-based multiblock grids to better conform to the round injector geometry, is under active investigation in the second year of the Stanford PSAAP-III Center.

3. Results

3.1. *Successful ignition case*

Cold fuel and oxidizer are injected into the combustion chamber for 2.9 ms prior to laser deployment, which is a sufficient time for recirculation zones to establish downstream of the injector, as indicated in Figure 4(a). The laser deposits an energy $E_L = 11.1\,\text{mJ}$ in the y direction while being focused at an axial distance $x_L = 12.7\,\text{mm} = 8R_o$ downstream of the injector and at a radial distance $y_L = 6.0\,\text{mm} = 3.8R_o$ from the centerline, in the vicinity of the shear layer formed by CH_4 and O_2. The laser deposition generates a kernel of hot gas with peak temperature 19,100 K, after which the gas expands while producing an outgoing blast wave that can be observed in Figure 4(a) at 5.3 μs after the pulse. The laser-generated kernel cools rapidly due to the expansion, and its temperature decreases to 8190 K by $t = 5.3\,\mu\text{s}$. For reference, the flow time scales based on the injector diameter and combustor length, using the initial O_2 inlet velocity, are $D/U_{O_2} = 21.5\,\mu\text{s}$ and $L_c/U_{O_2} = 377\,\mu\text{s}$, respectively.

The high temperature generated by the laser, along with a local composition that is within flammability limits, initiates combustion in the form of a turbulent premixed flame propagating outwardly in a concentration gradient. A nascent flame can be observed in Figure 4(b) at $t = 179\,\mu\text{s}$ after the pulse. The flow displacement created by the thermal

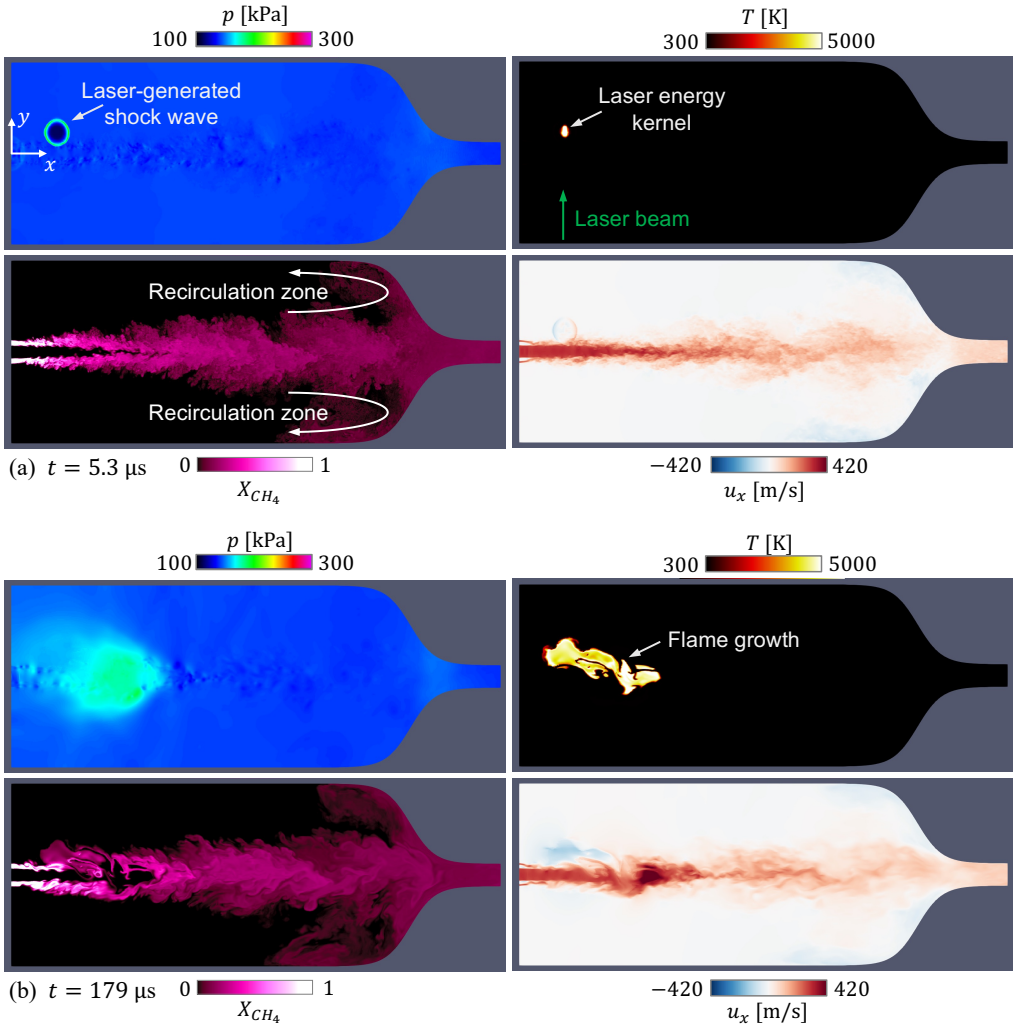

FIGURE 4. Instantaneous contours of pressure, temperature, CH_4 mole fraction, and x-velocity on the $z = 0$ centerplane at (a) $t = 5.3\,\mu s$ and (b) $t = 179\,\mu s$ after the laser-energy deposition. The pressure probe locations (see Figure 3) are out of plane and not visible in this cross section.

expansion creates a pressure wave spanning the width of the combustor and traveling in the streamwise direction toward the nozzle, as shown at $t = 302\,\mu s$ in Figure 5(a). The wave traverses the combustor and is partially reflected at the curved wall opposite the injector, resulting in a transient reversal of streamwise flow seen at $t = 466\,\mu s$ in Figure 5(b). The pressure time traces in Figure 6 indicate the first pass of the pressure wave over probes 1 and 3; the rise in pressure at probe 2 is delayed due to its location further downstream relative to probes 1 and 3. By $t = 570\,\mu s$ after the laser pulse, a turbulent diffusion flame occupies a significant portion of the combustor, whose mean pressure has risen 90 kPa above its pre-ignition value. Experimental observations (not shown in this report) indicate that the pressure continues to increase for another 100 ms (approximately 200 times the time period integrated here) before reaching a steady value

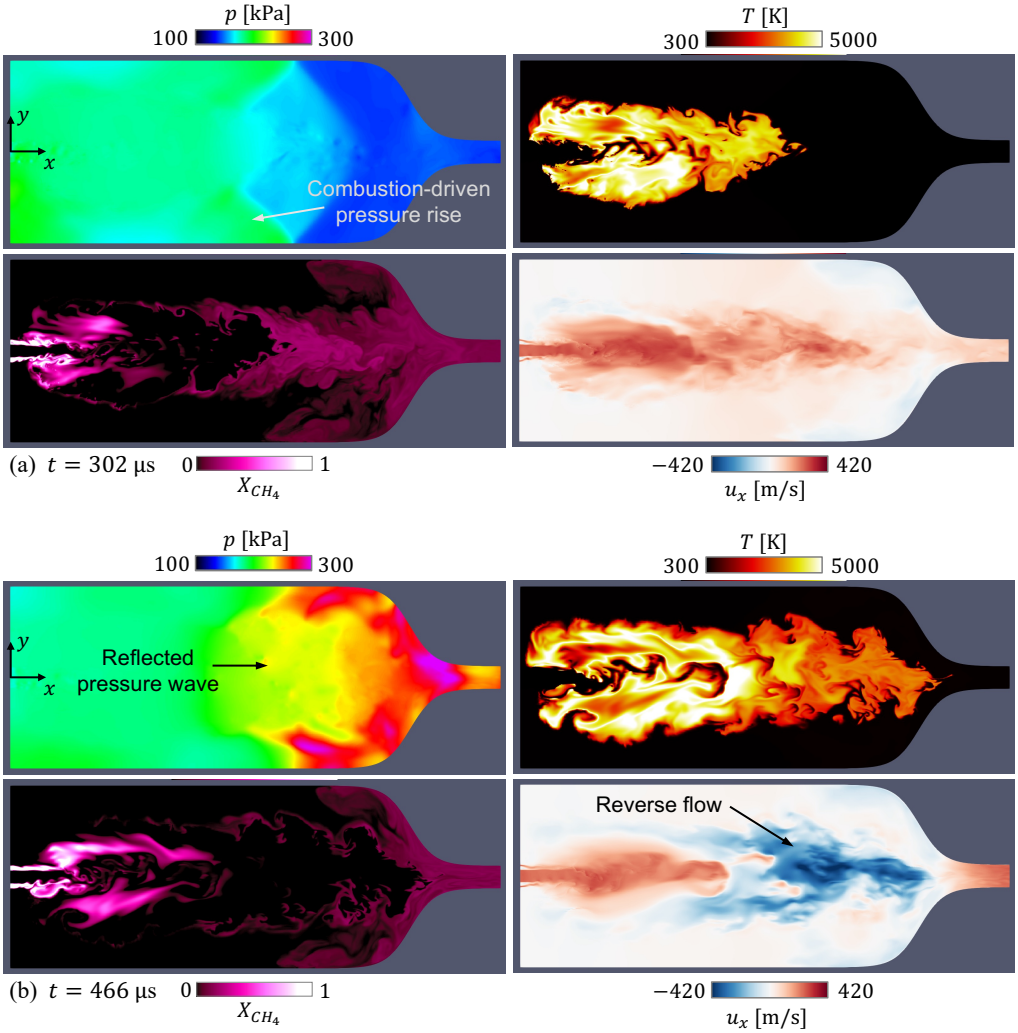

FIGURE 5. Instantaneous contours of pressure, temperature, CH_4 mole fraction, and x-velocity on the $z = 0$ centerplane at (a) $t = 302\,\mu s$ and (b) $t = 466\,\mu s$ after the laser-energy deposition. The pressure probe locations (see Figure 3) are out of plane and not visible in this cross section.

near 500 kPa. These considerations underscore the outstanding challenges associated with integrating the long time horizons required to achieve a steady post-ignition state in the combustor.

3.2. *Unsuccessful ignition case*

The effect of displacing the laser-energy deposition radially outwards and away from the shear layer is shown in Figure 7, which compares the instantaneous density contours of igniting and non-igniting cases. For the igniting case with $y_L = 6\,mm$, the same dynamics described in Section 3.1 can be observed in the density field. As shown in Figure 7(a), the energy deposition ignites the CH_4–O_2 shear layer, leading to flame growth, a low-density core region due to thermal expansion, and the formation of a longitudinal density wave as

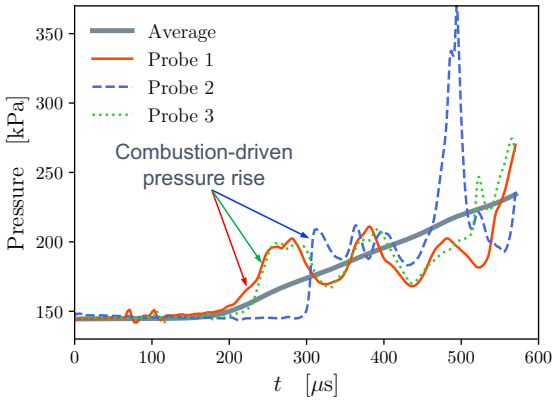

FIGURE 6. Time traces of the volume-averaged combustor pressure and local probe pressures for the successful ignition case (see Figure 3 for probe locations). The laser pulse occurs at $t = 0$.

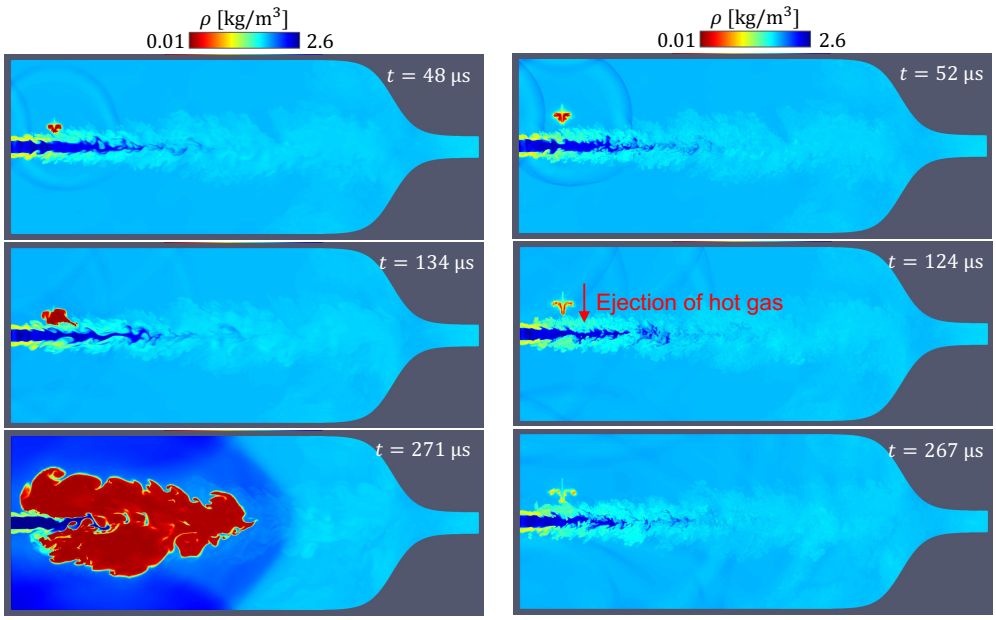

(a) $y_L = 6$ mm

FIGURE 7. Comparison of (a) ignition success with energy deposited at $y_L = 6\,\text{mm}$ from the centerline (case 4 in Table 2) and (b) ignition failure with energy deposited at $y_L = 7.5\,\text{mm}$ from the centerline (case 3). In both cases, the laser energy is deposited at $x = 12.7\,\text{mm} = 8R_o$ downstream of the injector.

a result of the flow displacement. However, moving the focal location radially outwards by 1.5 mm results in ignition failure, even when the gas absorbs more energy at this location. In both the igniting and non-igniting cases, the local mixture at the laser focal location is almost entirely O_2 and far too lean to ignite, but the expansion of the initially high-pressure kernel and the flow that this generates can distribute hot gas over a region whose size is comparable to the thickness of the shear layer, which can subsequently lead

Case	Laser focal location, y_L [mm]	Laser energy, E_L [mJ]	Ignition
1	12.0	21.0	No
2	9.0	21.0	No
3	7.5	22.8	No
4	6.0	11.1	Yes
5	3.0	8.2	Yes

TABLE 2. Cases simulated to construct the ignition map in Figure 8. In all cases, the laser energy is deposited at $x = 12.7\,\text{mm} = 8R_o$ downstream of the injector.

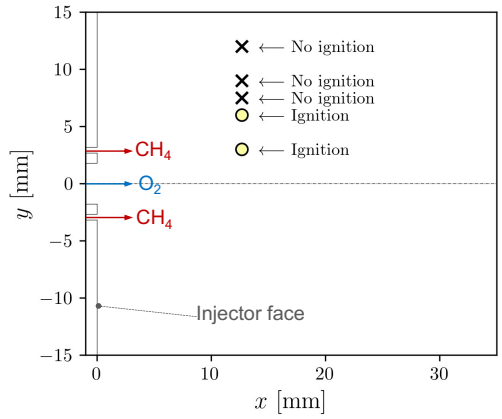

FIGURE 8. Spatial map of ignition outcome for the five cases listed in Table 2.

to ignition. For the laser beam orientation used in this configuration, this flow consists of an ejection of hot gas toward the CH_4/O_2 shear layer, which is a direct consequence of the asymmetric kernel geometry (figure 1) and results from vorticity-generating mechanisms early ($t \lesssim 10\,\mu$s) in its development (Glumac *et al.* 2005; Wang *et al.* 2021). While this occurs for both $y_L = 6\,$mm and $y_L = 7.5\,$mm, it is more clearly observed for the latter location (figure 7b), as the relatively small aerodynamic shear in that region leaves the laser-generated ejection largely undistorted.

3.3. *Ignition map*

In addition to investigating the dynamics of ignition, a primary objective is to identify the boundary between igniting and non-igniting cases. Five cases at varying laser y-locations, summarized in Table 2, are used to construct a spatial map of the ignition outcome, shown in Figure 8. The laser energy absorbed by the gas (E_L in Table 2) depends on flow properties in the focal region and is measured in the parallel experimental validation effort. Ignition can be determined on the basis of the time trace of various quantities, such as the combustor mean temperature and total mass of H_2O vapor produced by the combustion, as shown in Figure 9. For non-igniting cases, the combustor mean temperature remains close to its ambient value. Ignition tends to fail as the laser focal location is moved radially outwards, consistent with experimental observations not reported here.

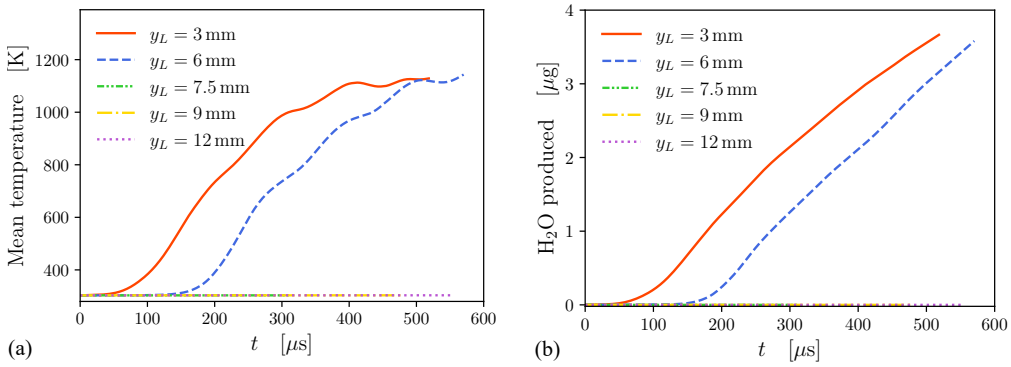

FIGURE 9. Time traces of (a) combustor mean temperature and (b) total mass of H_2O produced for all cases listed in Table 2. The laser pulse occurs at $t = 0$.

	Pre-ignition	Post-ignition
Time step	16 ns	4–13 ns
Wall-clock time per time step	0.46 s	0.68 s
Number of time steps	180,000	100,000
Physical time integrated	2.9 ms	0.57 ms
Total wall time	23 hrs	19 hrs

TABLE 3. Simulation cost of pre-ignition and post-ignition stages.

3.4. *Code performance*

The simulations described above were run with the task-based solver on 12 nodes of Lassen Supercomputer at Lawrence Livermore National Laboratory (LLNL). Each Lassen node has 40 IBM Power9 processors and 4 NVidia V100 GPUs. Table 3 provides the computational cost of the simulations. While the time step of the pre-ignition flow was limited by acoustics. the time step of the post-ignition flow was limited by chemistry and became increasingly smaller as the chamber pressure increased. Additionally, a small time step $\Delta t = 0.2$ ns was used to resolve the flow around the time of laser-energy deposition, although this period led only to a small portion of the overall computational cost due to its short duration.

As shown in Figure 10, the code performance was demonstrated by an efficiency larger than 90% in weak scaling up to 64 nodes with 40 million grid points per node using the same grid topology, numerical discretizations, and physical models described in Sections 2.2 and 2.3. The results show a degradation of parallel efficiency of approximately 10% with respect to a similar test conducted by Di Renzo *et al.* (2020) using a prior release of the code and a previous release of Legion. Investigations are currently underway to address this behavior with a detailed profile of the solver.

4. Concluding remarks and ongoing work

Progress on simulations of laser ignition in a CH_4/O_2 model rocket combustor using a multi-GPU task-based solver during the first year of the Stanford PSAAP-III Center has been reported. Combustor-scale dynamics are described and shown to be consistent

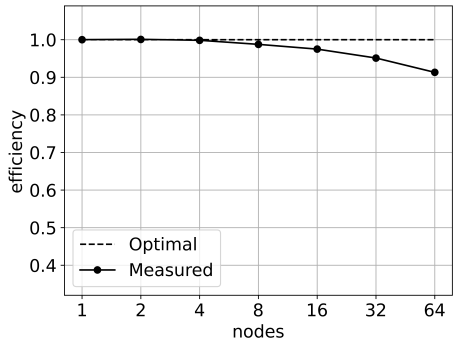

FIGURE 10. Weak scaling on Lassen up to 64 nodes with 40 million grid points per node. In this figure, efficiency is defined by the wall-clock time per simulation time step divided by the corresponding wall-clock time using 1 node.

with the chamber pressure evolution. Both igniting and non-igniting cases are identified to construct a spatial map of the ignition response, indicating the ignition boundary in the radial direction. The task-based solver can performed these calculations with more than 90% efficiency up to 64 nodes.

Several areas are under active investigation in the second year of the Stanford PSAAP-III Center. Incorporation of subgrid-scale and turbulent-combustion models with appropriate discretization strategies to address the significant resolution requirements is a primary focus. In order to conduct rigorous comparisons with experiments, ongoing efforts are also focused on quantifying and propagating uncertainties, including those arising not only from modeling parameters and assumptions but also from inherently stochastic elements of the system, such as run-to-run variation in the inflow and absorbed laser energy. More elaborate models for the laser-energy deposition, particularly radiative and plasma-kinetic mechanisms that mediate it, are also under consideration. In order to minimize discrepancies between the simulation and experimental geometries, Legion-based multiblock grid capabilities are under active development, with particular attention to computational performance under the multiphase conditions necessary for eventual operation of the combustor with LOX sprays.

Acknowledgments

This investigation was funded by the Advanced Simulation and Computing (ASC) program of the US Department of Energy's National Nuclear Security Administration (NNSA) via the PSAAP-III Center at Stanford, Grant No. DE-NA0002373. C.W. was funded by a Stanford School of Engineering Graduate Fellowship. The authors are grateful to Dr. Charlelie Laurent for useful comments, and to Mr. Ryan Strelau and Prof. Carson Slabaugh from Purdue University for stimulating connections with the experimental validation effort.

REFERENCES

ALBERTI, A., MUNAFÒ, A., KOLL, M., NISHIHARA, M., PANTANO, C., FREUND, J. B., ELLIOTT, G. & PANESI, M. 2020 Laser-induced non-equilibrium plasma kernel dynamics. *J. Phys. D Appl. Phys.* **53**, 025201.

Bauer, M., Treichler, S., Slaughter, E. & Aiken, A. 2012 Legion: Expressing locality and independence with logical regions. *In SC '12: International Conference for High Performance Computing, Networking, Storage and Analysis*.

Brieschenk, S., O'Byrne, S. & Kleine, H. 2014 Ignition characteristics of laser-ionized fuel injected into a hypersonic crossflow. *Combust. Flame* **161**, 1015–1025.

De Oliveira, P. M., Allison, P. M., Mastorakos, E. 2002 Ignition of uniform droplet-laden weakly turbulent flows following a laser spark. *Combust. Flame* **199**, 387–400.

Di Renzo, M., Fu, L. & Urzay, J. 2020 HTR solver: An open-source exascale-oriented task-based multi-GPU high-order code for hypersonic aerothermodynamics. *Comput. Phys. Commun.* **255**, 107262.

Di Renzo, M. & Urzay, J. 2021 Direct numerical simulation of a hypersonic transitional boundary layer at suborbital enthalpies. *J. Fluid Mech.* **912**, A29.

Eyssartier, A., Cuenot, B., Gicquel, L.Y., Poinsot, T. 2013 Using LES to predict ignition sequences and ignition probability of turbulent two-phase flames. *Combust. Flame* **160**, 1191–1207.

Fernández-Tarrazo, E., Sánchez, A.L, Liñán, A. & Williams, F.A. 2006 A simple one-step chemistry model for partially premixed hydrocarbon combustion. *Combust. Flame* **147**, 32–38.

Fong, C. 2018 Squircular calculations. *in Joint Mathematics Meeting, SIGMAA-ARTS.*

Fu, L., Hu, X. Y. & Adams, N. A. 2016 A family of high-order targeted ENO schemes for compressible-fluid simulations. *J. Comput. Phys.* **305**, 333–359.

Gottlieb, S., Shu, C.-W. & Tadmor, E. 2001 Strong stability-preserving high-order time discretization methods. *SIAM Rev.* **43**, 89–112.

Hu, X., Adams, N. & Shu, C. 2013 Positivity-preserving method for high-order conservative schemes solving compressible Euler equations. *J. Comput. Phys.* **242**, 169–180.

Glumac, N. G., Elliott, G. S. & Boguszko, M. 2005 Temporal and spatial evolution of a laser spark in air. *AIAA Journal* **43**, 1984–1994.

Jo, S. & Gore, J.P. 2022 Laser ignition energy for turbulent premixed hydrogen air jets. *Combust. Flame* **236**, 111767.

Kroupa, G. & Börner, M. 2018 A miniaturized high energy laser for ignition of rocket engines. *in International Conference on Space Optics—ICSO*.

Kurdyumov, V., Blasco, J., Sánchez, A.L. & Liñán, A. 2004 On the calculation of the minimum ignition energy. *Combust. Flame* **136**, 394–397.

Lacaze, G., Cuenot, B., Poinsot, T. & Oschwald, M. 2009 Large eddy simulation of laser ignition and compressible reacting flow in a rocket-like configuration. *Combust. Flame* **156**, 1166–1180.

Manfletti, C. 2014 Laser ignition of an experimental cryogenic reaction and control thruster: pre-ignition conditions. *J. Propul. Power* **30**, 925–933.

Marrero-Santiago, J., Collin-Bastiani, F., Riber, E., Cabot, G., Cuenot, B. & Renou, B. 2020 On the mechanisms of flame kernel extinction or survival during aeronautical ignition sequences: Experimental and numerical analysis. *Combust. Flame* **222**, 70–84.

Mayer, J. E. & Mayer, M. G. 1959 *Statistical Mechanics*. Wiley, New York.

MacArt, J. F., Wang, J. M., Popov, P. P. & Freund, J. B. 2021 Detailed simu-

lation of laser-induced ignition, spherical-flame acceleration, and the origins of hydrodynamic instability. *Proc. Combust. Inst.* **38**, 2341–2349.

McBride, B. J., Zehe, M. J. & Gordon, S. 2002 *NASA Glenn coefficients for calculating thermodynamic properties of individual species.* NASA TP # 2002-211556.

Melcher, J. C. & Morehead, R. L. 2014 Combustion stability characteristics of the project Morpheus liquid oxygen/liquid methane main engine. *in 50th AIAA/ASME/SAE/ASEE Joint Propulsion Conference*.

Morsy, M. H. & Chung, S. H. 2002 Numerical simulation of front lobe formation in laser-induced spark ignition of CH4/air mixtures. *Proc. Combust. Inst.* **29**, 1613–1619.

Munafò, A., Alberti, A., Pantano, C., Freund, J. B. & Panesi, M. 2019 A computational model for nanosecond pulse laser-plasma interactions. *J. Comput. Phys.* **406**, 109190.

Okong'o, N. & Bellan, J. 2002 Consistent boundary conditions for multicomponent real gas mixtures based on characteristic waves. *J. Comput. Phys.* **176**, 330–344.

Panchapakesan, N. R. & Lumley, J. L. 1993 Turbulence measurements in axisymmetric jets of air and helium. Part 1. Air jet. *J. Fluid Mech.* **246**, 197–223.

Phuoc, T. X. 2006 Laser-induced spark ignition fundamental and applications. *Opt. Lasers Eng.* **44**, 351–397.

Phuoc, T. X. & White, F. P. 2002 An optical and spectroscopic study of laser-induced sparks to determine available ignition energy. *Proc. Combust. Inst.* **29**, 1621–1628.

Poinsot, T. J. & Lele, S. K. 1992 Boundary conditions for direct simulations of compressible viscous flows. *J. Comput. Phys.* **101**, 104–129.

Pope, S. B. 2000 *Turbulent Flows*, Cambridge University Press.

Slaughter, E., Lee, W., Treichler, S., Bauer, M. & Aiken, A. 2015 Regent: A high-productivity programming language for HPC with logical regions. *In SC '15: Proceedings of the International Conference for High Performance Computing, Networking, Storage and Analysis*.

Wang, J. M., Buchta, D. A. & Freund, J. B. 2020 Hydrodynamic ejection by laser-induced optical breakdown. *J. Fluid Mech.* **888**.

Wang, J. M., MacArt, J. F. & Freund, J. B. 2021 Flow dynamics of laser-induced breakdown at a fuel–oxidizer interface and its effect on ignition. *Combust. Flame* **229**, 111375.

Wermer, L., Hansson, J. & Im, S.-K. 2017 Dual-pulse laser-induced spark ignition and flame propagation of a methane diffusion jet flame. *Proc. Combust. Inst.* **36**, 4427–4434.

Harilal, S. S., Brumfield, B. E. & Phillips, M. C. 2015 Lifecycle of laser-produced air sparks. *Phys. Plasmas* **22**, 063301.

Zeldovich, Y.B. & Raizer, Y.P. 1966 *Physics of Shock Waves.* Dover.